Renewable Energy
August 2022, Volume 196 Pages 1204-1217
https://doi.org/10.1016/j.renene.2022.07.050
https://archimer.ifremer.fr/doc/00787/89864/

Experimental investigation of the upstream turbulent flow modifications in front of a scaled tidal turbine

Druault Philippe [1, *], Germain Gregory [2]

[1] Sorbonne Université, CNRS, Institut Jean Le Rond d'Alembert, F-75005, Paris, France
[2] Ifremer, Marine Structure Laboratory, 150 quai Gambetta, 62200, Boulogne-sur-mer, France

* Corresponding author : Philippe Druault, email address : philippe.druault@sorbonne-universite.fr

gregory.germain@ifremer.fr

Abstract :

A 1:20 scaled three-bladed horizontal-axis tidal turbine is positioned in the wake flows of two wall-mounted obstacles: a square cylinder and a combination of a cube in front of a cylinder. The turbine's induction effects are examined with upstream flow measurements without and with the turbine operating at its optimal regime. In front of the turbine (at 0.07D upstream of the hub extremity, with D the turbine diameter), the mean axial and vertical velocities are modified by induction effects whatever the complexity of the flow is. In the other hand, the normal Reynolds tensor components are less impacted by the turbine's blockage. In the presence of an incoming uniform homogeneous Gaussian flow field, a mean axial velocity deficit of 30% is observed in front of the hub while this velocity deficit is around 10% at the rotor edge. Moreover, the turbine's blockage modifies the intermittency leading to non-Gaussian fluctuations. When low-frequency large-scale flow structures are embedded in the incoming turbulent flow, these large-scale flow structures are affected by the hub whereas the rotating blade's blockage effect is of minor contribution. In this case, the turbine does not affect significantly the intermittency.

Keywords : Tidal turbine, Blockage effect, Turbulence, Intermittency, PIV

1. Introduction

An important challenge for the development and the exploitation of renewable wind or tidal energy is to accurately predict the mean turbine performances and its associated fluctuations. Power and thrust coefficients are commonly expressed as a function of a reference averaged velocity. For wind turbine industrial applications, the International Electrotechnical Commission [25] recommends to use the time average wind speed measured at hub height, at least 2 diameters upstream of the rotor where turbine's induction is negligible. Similarly, for tidal turbine, a mean reference velocity has to be measured upstream of the turbine outside the turbine induction area [24, 18]. However, such a reference velocity may be not

fully representative of an accurate description of the flow that impacts the rotor. Previous analysis of a laboratory scale tidal turbine proposed to consider as reference velocity the one measured at the turbine position but without the turbine [4, 20]. In-situ solution consists in measuring the velocity inside the turbine induction region by performing Lidar measurements mounted on a wind turbine nacelle [45, 46] or super-large-scale Particle Image Velocimetry (PIV) measurements [32]. Some questions were also raised recently to correct this reference velocity by taking into account the turbine farm environment, the so-called wind farm global-blockage effect. It was observed that downstream turbines or neighboring turbines influence upstream turbines by modifying its performance [48, 43, 29]. The blockage effect in laboratory experiments can be taken into account to improve the turbine performance assessments [1, 30]. A key issue concerns also the characterization of the region where the flow is decelerated in front of the turbine which is referred to the upstream turbine induction area or turbine blockage area. As we know that the turbine performance parameters and its associated fluctuations are dependent on the environmental conditions (shear velocity profile, turbulence intensity, integral length scales, Gaussian or non-Gaussian turbulence statistics) [50, 5, 20, 16], it is of importance to quantify how incoming turbulent flows are affected by the turbine's presence.

The analysis of this upstream flow area remains complex due the difficulty in experimentally measuring the spatio-temporal flow dynamics in front of a turbine and/or in carrying out numerical simulations that can reproduce a realistic unsteady Fluid-Structure Interaction (FSI) [42, 13, 9]. Furthermore, many advanced numerical simulations are based on the simplified actuator-disk or -line methods to model the rotor [38, 7]. Even if this simplification allows a great understanding of the behavior of wind and tidal turbines, especially their wake development, such a model presents some important limitations for the characterization of the flow in front of the rotor. Upstream flow is assumed to be steady and generally spatially uniform even if recent shear mean flow were considered [40]. To characterize the turbine induction area, some analytical velocity deficit law called induction area model, can be used [10]. This allows for the flow deceleration along the axial rotor-axis to be taken into account. Experimentally, this induction zone model was regarded with varying degrees of success [39, 2, 45, 12, 33, 47]. Based on a scaled or in-situ wind turbine, recent experimental measurements of the mean streamwise velocities along the rotor axis, in the upstream region of a single turbine with zero yaw angle were performed. Some showed a good agreement between velocity deficit law and experimental measurements [2, 33, 47] while some differences were noted in other previous measurements [39, 45, 23]. It also clearly shown how the upstream flow is affected by the presence of the hub and increases with tip speed ratio [31]. The modification of turbulence in front of the actuator disk model was also studied [38] but the use of a simple quasi-steady actuator disk model can not allow to conclude on such an effect, neither by means of Synthetic-Eddy-Method coupled with a simplified turbine model [9]. A semi-analytical model taking into account the distortion of incoming homogeneous turbulence was also recently proposed [11].

The purpose of this work is to study the turbine's blockage effect in a high

Reynolds number turbulent flow and to analyze how a turbine alters the properties of the incoming turbulent flow. Magnier et al. [35] recently investigated the shear (with classical power law) effect on the turbine behavior. They found that the phase average of the load and the velocity perceived by the blades are highly correlated with a phase lag dependent on the turbine rotational speed and on the incoming flow shear. This effect was attributed to potential induction effects. In this work we propose to identify the induction effects in a complex turbulent shear flow containing large scale flow structures encountered in the wake of wall-mounted obstacles. An experimental analysis of the turbine induction zone is then conducted from a laboratory 1:20 scaled tidal turbine subjected to various turbulent flow conditions such as the wake of some wall-mounted obstacles. Even if this laboratory test can not reproduce fully complex realistic conditions, these kinds of experiments are fully controllable. Thus, it will be possible to address the discrepancies between the turbulent flow in front of the turbine and its corresponding turbulent free flow, in the absence of the turbine at the same location. This paper is organized as follows. The turbulent flow configurations and the measurement methods are presented in section 2. A first analysis of the turbine's blockage effect is conducted from an incoming uniform or slightly shear flow in section 3. Then, section 4 presents the turbine's induction modifications in a more complex turbulent shear flow containing large scale flow structures. Finally, a brief summary and discussion of our main findings are presented in Section 5.

2. Experimental database

2.1. Experimental set-up and measurement methods

Two configurations of wall-mounted obstacles are considered to mimic the effect of bathymetry observed at Alderney Race in the middle of the English Channel, which is a potential site in French water [49]. The first one (denoted $C6$) is a wall bottom-mounted square cylinder of height $H = 0.25$m and of length $6H$ [27], and the second one (denoted $C1C6$) is the same wall mounted cylinder but with a cube of height H located $2H$ upstream the cylinder [37]. The obstacles are positioned at the test section center, symmetrically around the spanwise origin $y = 0$.

The wave and current circulating flume tank of IFREMER is presented in figure 1 (top), where the main dimensions are indicated. The surface-mounted obstacles are positioned in similar inflow conditions imposed at inlet: a uniform incoming flow ($U_\infty = 1\text{m.s}^{-1}$, $V_\infty = 0$, $W_\infty = 0$) along the (x, y, z) directions respectively, with a low turbulence intensity, of $I_\infty = 1.5\%$. The Reynolds number $U_\infty H/\nu$ is equal to 2.5 10^5. The Froude number $U_\infty/\sqrt{gh}$ is equal to 0.23 with $h = 2$m the depth of the water column. The upstream flow is a hydrodynamically smooth wall boundary layer. The boundary layer height is of $\delta^* = \delta/H = 1.3$ at the obstacle location [28, 26]. Figure 1 displays the experimental mean velocity profile of the boundary layer flow. This profile is compared to classical power law velocity profiles $\overline{U} = U_\infty\,(z/h)^{1/\alpha}$. It is observed that in the lower part of the flume tank $z^* = z/H < 1$ the boundary layer velocity profile approaches some

classical ones when using $U_\infty = 1.3\text{m.s}^{-1}$ and $6 \leq \alpha \leq 7$. This flow then interacts with wall mounted obstacles and two different wake flows are obtained. The previous investigations have shown that $C6$ wake flow presents some Large Scale flow Structures (LSS) that are shed by the obstacle and then self-organized in the water column [28] while $C1C6$ wake flow is different as the upstream cube effect prevents any flow structures to rise in the water column [37]. The Strouhal number $S_t = fH/U_\infty$ associated with the frequency passage of the large scale flow structures in the $C6$ far wake is equal to 0.06 [28]. To study the blockage effect on the incoming flow, a 1:20 scaled tri-bladed horizontal axis tidal turbine is successively positioned at four streamwise locations: $x^* = x/H = 4,\ 10,\ 16,\ 23$ in the wake of both flow configurations. The x-origin coincides with the x-center of the cylinder (see figure 1). The turbine has a diameter $D = 0.724$m and its center is located at mid-depth ($z^* = 4$) and mid-span ($y^* = 0$) in the tank ($D/H = 2.89$). In this work, the turbine is at its nominal operating point [36], with a Tip Speed Ratio of $TSR = \frac{\omega R}{U_\infty} = 4$, where $R = D/2$ is the rotor radius and ω the angular velocity. In the following, the measurements carried out in front of the turbine will be indexed by $TSR4$. Note that even if the surface mounted obstacles constitute a blockage ratio of 4.5% in the basin, this will not impact the next analysis of the turbine's blockage effect. Indeed, the comparison analysis will be done from free (without any turbine) and TSR4 flow configurations which are based on the same incoming turbulent flow.

Particle Image Velocimetry (PIV) technique is implemented to measure instantaneous velocity vector fields (streamwise and vertical velocity components, u and w) in a vertical plane $(x, y = 0, z)$ in front of the turbine (figure 1) at each x-section. This plane is centered vertically at hub height and ends horizontally at the blade edge. It is discretized on 330×840 pixels^2, corresponding to a physical meshgrid of $(N_x \times N_z) = (30 \times 74)$ with a spatial discretization of 11.2mm. The measurement time duration is $T = 180$s with a sampling frequency of 15Hz. To investigate the upstream flow property alterations due to the turbine, similar PIV measurements are performed in a free flow (without any turbine), at the same x-section. Due to shadowing effect in the measurement plane, the instantaneous velocity components (u, w) extracted along a vertical line (N_z points) at the x-centered of the PIV plane are only retained for the next analyses. This vertical line is located at $0.07D = 0.05$m upstream of the hub extremity. Note that previous investigations obtained with the same turbine as ours in the same experimental set-up, but with an upstream homogeneous turbulent flow with a turbulence intensity of 13% shown that the mean velocity remains unchanged up to 1D along the hub axis [11].

As stated in the introduction part, in-situ conditions require the velocity measurements at least at 2D upstream of the operating turbine, to access a representative mean reference velocity. For future comparisons, Laser Doppler Velocimetry (LDV) measurements are implemented to measure a reference velocity at a single point located two rotor diameters upstream and at the hub height ($z^* = 4$). These LDV measurements are carried out using a 2D Dantec Fiberflow system and allow the measurements of instantaneous velocity components at a frequency varying from 200 to 300Hz depending on the number of particles passing through

	C1C6			
	4	10	16	23
$\overline{U}_{LDV}$	1.05	1.07	1.03	1.01
C_p	0.44	0.37	0.42	0.42
C_T	0.92	0.83	0.90	0.91
a	0.36	0.30	0.34	0.35

	C6			
	4	10	16	23
$\overline{U}_{LDV}$	1.00	1.09	1.03	0.97
C_p	0.53	0.35	0.36	0.40
C_T	1.03	0.79	0.82	0.90
a	-	0.27	0.29	0.34

Table 1: Values of the thrust and power coefficient in each x-section based on the reference velocity $\overline{U}_{LDV}$. The values of the associated induction factor $a = \frac{1}{2}\left(1 - \sqrt{1 - C_T}\right)$ are also indicated. Left hand side: C1C6 flow configuration. Right hand side: C6 flow configuration. At $x^* = 4$, the induction factor a can not be evaluated as $C_T > 1$.

the measurement volume [19].

Table 1 details the experimental values [36, 15] of the time average thrust and power coefficients in each x-section for both flow configurations. These coefficients are computed from the reference mean velocity measured with LDV, $\overline{U}_{LDV}$ as follows:

$$C_T = \frac{\overline{T}}{0.5\rho A \overline{U}_{LDV}^2} \quad \text{and} \quad C_p = \frac{\omega \overline{M}}{0.5\rho A \overline{U}_{LDV}^3} \tag{1}$$

where $A = \pi R^2$ is the rotor swept area, ρ the fluid density equal to 1000kg.m^{-3}, $\overline{T}$ and $\overline{M}$ are the measured time average turbine thrust and torque respectively. To characterize the induction effect, the induction factor is estimated as $a = \frac{1}{2}\left(1 - \sqrt{1 - C_T}\right)$ by applying momentum theory for a turbine with zero yaw angle. The values of the associated induction factor are also indicated in this table. These values will be used for the following analytical comparisons.

The reader is referred to previous works [27, 17, 19, 14, 37] and references therein, for details about experimental set-up, the measurement method implementation, the acquisition parameters and the associated measurement errors.

2.2. Global mean characterization of both wake flows

Previous studies presented in details both $C6$ and $C1C6$ wake flow configurations [28, 27, 17, 37]. Figure 2 displays the mean streamwise $\overline{U}$ velocity component, in the y-centered plane for both configurations without any turbine. $\overline{U}$ is deduced from classical Reynolds Decomposition: $u(t, \mathbf{X}) = \overline{U(\mathbf{X})} + u'(t, \mathbf{X})$, u' being the associated fluctuating component. The vertical blue lines indicate the four turbine locations of the functioning turbine in the following experiments. The index $free$ used in the following will be associated with flow variables measured in free flow in the absence of the turbine. The black line representation in figure 2 corresponds to $\overline{U}_{free} = 0.9U_\infty$. The spatial development of the wake flow differs as a function of the configuration. Indeed, the presence of an upstream cube ($C1C6$ case) prevents the vertical development of the wake [37]. Consequently, whatever the turbine locations in the $C1C6$ wake flow, a quasi-similar mean streamwise flow is observed. From $z^* > 4$ the mean flow is uniform and constant, corresponding to the incoming flow U_∞. Below $z^* < 4$, a small shear flow is present associated with the horizontal wake flow development.

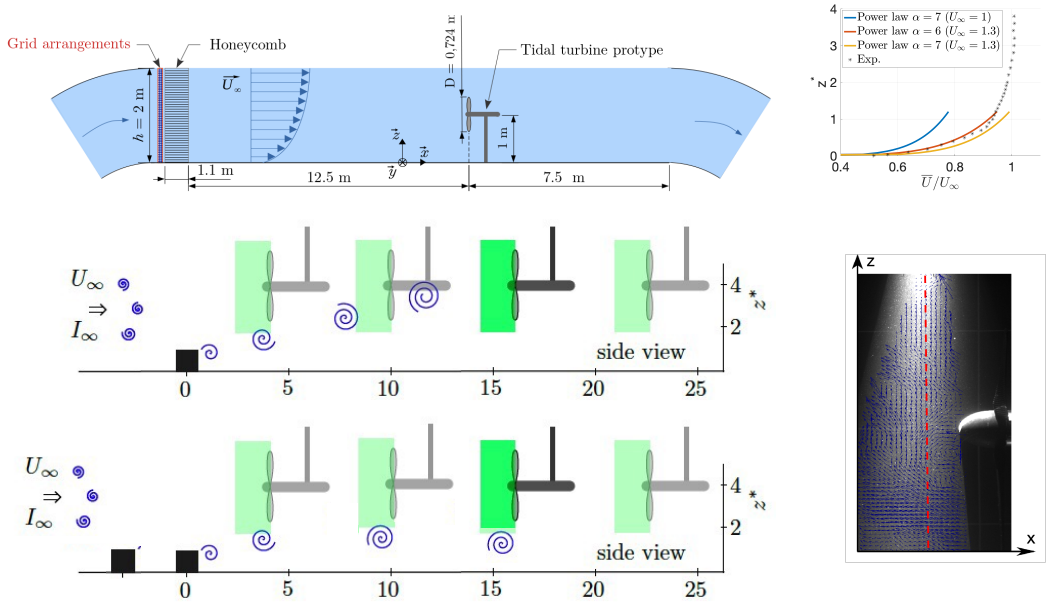

Figure 1: Top-Left: Illustration of the experimental set-up without wall-mounted obstacles. Top-right: Experimental boundary layer mean velocity profile, superimposed onto power law velocity profiles. Bottom-Left: Locations of turbine and PIV vertical measurement planes, wall-mounted cylinder configuration (top) and wall-mounted obstacles in tandem configuration (bottom). Bottom-Right: Illustration of an instantaneous velocity vector measurement and the location of the vertical line under consideration (red dashed line).

For the $C6$ flow configuration, at $x^* = 4$ the mean streamwise flow field is quasi-uniform with a slight flow acceleration area at $z^* \in [3 : 4]$. Far downstream, at $x^* = 10, 16, 23$, the mean streamwise velocity profiles exhibit some noticeable vertical shear profiles.

As previously presented [28, 17, 37], the mean vertical velocity component, $\overline{W}_{free}$, exhibits globally similar zero values in each streamwise section for both flow configurations. It is directly related to the two-dimensional nature of the flow in this y-centered plane.

3. Turbine induction effect in a uniform or slight shear flow

The $C1C6$ flow configuration is firstly examined as a similar slight shear velocity profile with a low level of turbulence is obtained at the four turbine locations. A comparative analysis of the mean velocity field and the normal Reynolds tensor components is performed by exploiting one-point LDV measurements at 2D upstream of the turbine location and PIV measurements along a vertical line just in front of the rotor location with or without the turbine.

3.1. Turbine blockage effect on the mean velocity components

In each streamwise section, the mean streamwise velocity component $\overline{U}$ is calculated along the vertical rotor diameter ($z^* \in [2.56 : 5.44]$), at $y = 0$ (figure 3 - left). Dashed-lines correspond to the $\overline{U}_{free}$ component, while solid-lines

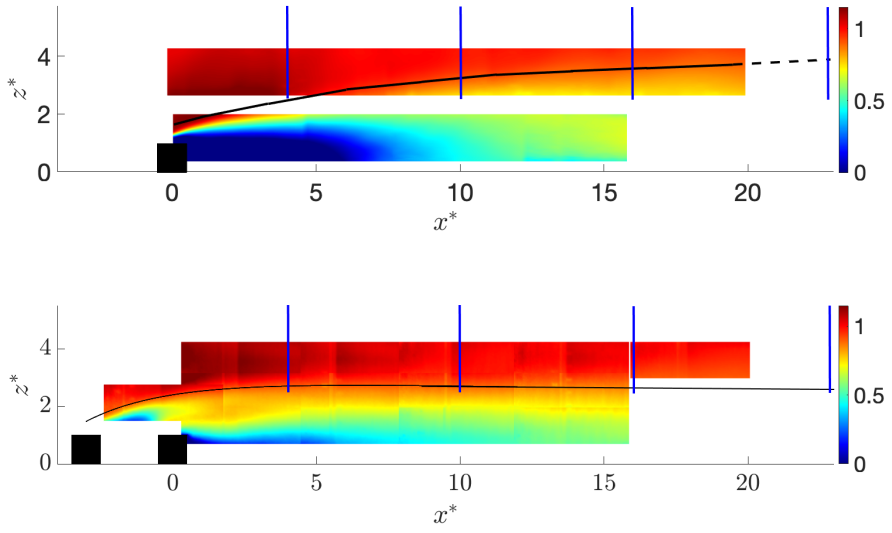

Figure 2: $C6$ (top) and $C1C6$ (bottom) wake flow configurations. Mean streamwise ($\overline{U}_{free}$) velocity component in the symmetrical $y = 0$ plane. Black line indicates the location where $\overline{U}_{free} = 0.9U_\infty$. Blue lines indicate the locations of the turbine: $x^* = 4$, $x^* = 10$, $x^* = 16$ and $x^* = 23$.

correspond to mean flow component $\overline{U}_{TSR4}$ in front of the turbine. As stated before, in the free flow, at height $z^* \in [4 : 5.5]$, the mean streamwise velocity field is quasi-uniform while a shear is observed at the bottom part of the turbine highlighting the wake expansion in the symmetrical plane. The one-point LDV measurements (see table 1) can not recover the shear profile observed at the bottom part $z^* \in [2.5 : 4]$.

The free mean flow profiles are compared to those measured in the Alderney Race [44] where the velocity profile follows the power law:

$$\overline{U} = U_{ref} \left(\frac{z}{D_e} \right)^{1/\alpha} \tag{2}$$

with U_{ref} the velocity at mean depth, D_e the depth of water column and z the distance from the bottom. In this area, it was found that α is between 4 and 14. Here, D_e is equal to $h = 2$m (see figure 1). Present mean free velocity profiles exhibit a similar power law profile ($\alpha = 4$), in the lower half ($z^* < 4$), for each streamwise section. This is in agreement with the in-situ observations.

When regarding the mean profiles in front of the turbine whatever the x-section is, the velocity deficit is clearly indicated in this induction zone with a lower induction in front of the rotating blades. These profiles are consistent with previous PIV and Lidar measurements carried out in a horizontal and/or vertical planes upstream of a wind turbine [39, 45, 22, 2, 33]. The most important mean deficit is around the hub obstacle, that creates two vertical shear profiles above and below the hub. It is interesting to note that incoming uniform constant flow or

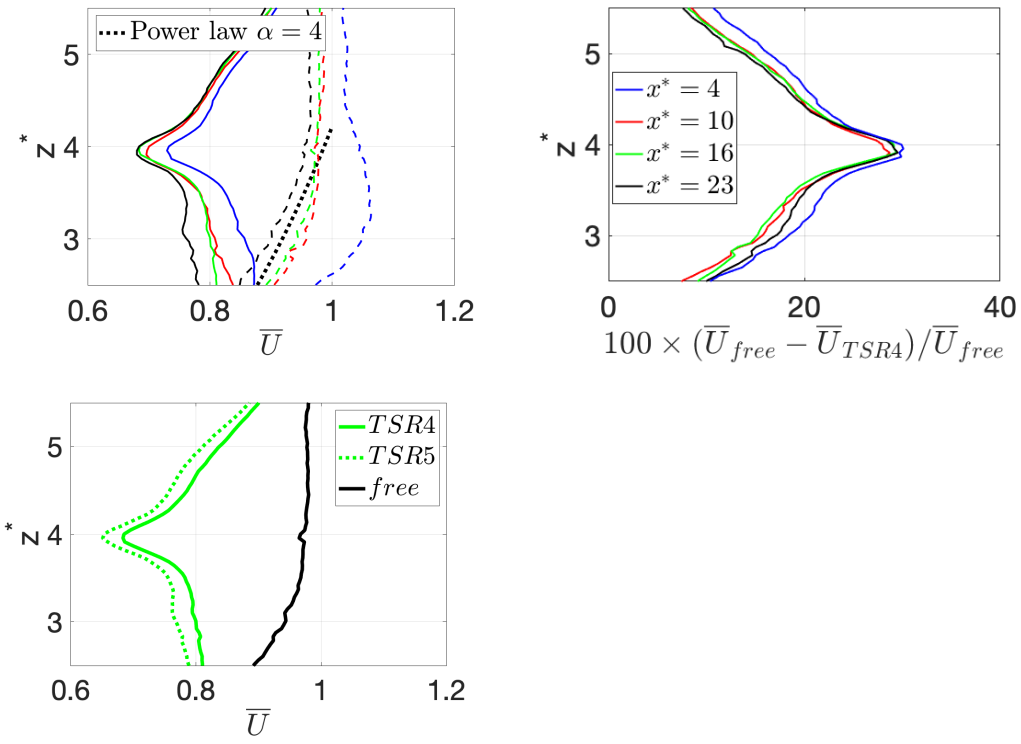

Figure 3: $C1C6$ flow configuration. Top-Left: Superimposition of the vertical z-profiles of the mean streamwise $\overline{U}$ velocity component, for the four turbine locations: $x^* = 4$ (blue), $x^* = 10$ (red), $x^* = 16$ (green), $x^* = 10$ (black). The lines and dashed-lines correspond $\overline{U}_{TSR4}$ and $\overline{U}_{free}$ respectively. Power law velocity profile is also indicated with dotted line. Top-Right: Velocity deficit expressed as percentage values, $100 \times \left(\overline{U}_{free} - \overline{U}_{TSR4}\right)/\overline{U}_{free}$. Bottom-left: Comparison of the mean flow deficit at two rotational speeds: the optimal functioning point TSR4 and at TSR=5 ($x^* = 16$).

low shear flow leads to similar both shear profiles in front of the turbine. The shear profile is accentuated below the hub height by comparison with the one above, due to the main existing free shear flow across the bottom part of the turbine. However, a great symmetry about the turbine is obtained when regarding the velocity deficit (figure 3 - top-right), expressed as a percentage value as follow:

$$100 \times \left(\overline{U}_{free}(z) - \overline{U}_{TSR4}(z)\right)/\overline{U}_{free}(z) \tag{3}$$

Whatever the streamwise section is, the velocity deficit lies around 7% and 11% at the edge of the rotor and it is maximal in front of the hub approaching $\sim 30\%$. These values are quite higher than those obtained from previous velocity deficit measurements in front of a wind turbine [45]. An estimation of the mean flow deficit is between 10% and 20% for the last 25% of the blade length for which most of the turbine power is generated. Note that this percentage deficit is predominantly governed by rotational speed. Thus, we conducted a similar experiment at $x^* = 16$ but using the turbine rotational $TSR = 5$. Figure 3 (bottom-left) compares the associated mean flow deficit to the one obtained at the optimal operating

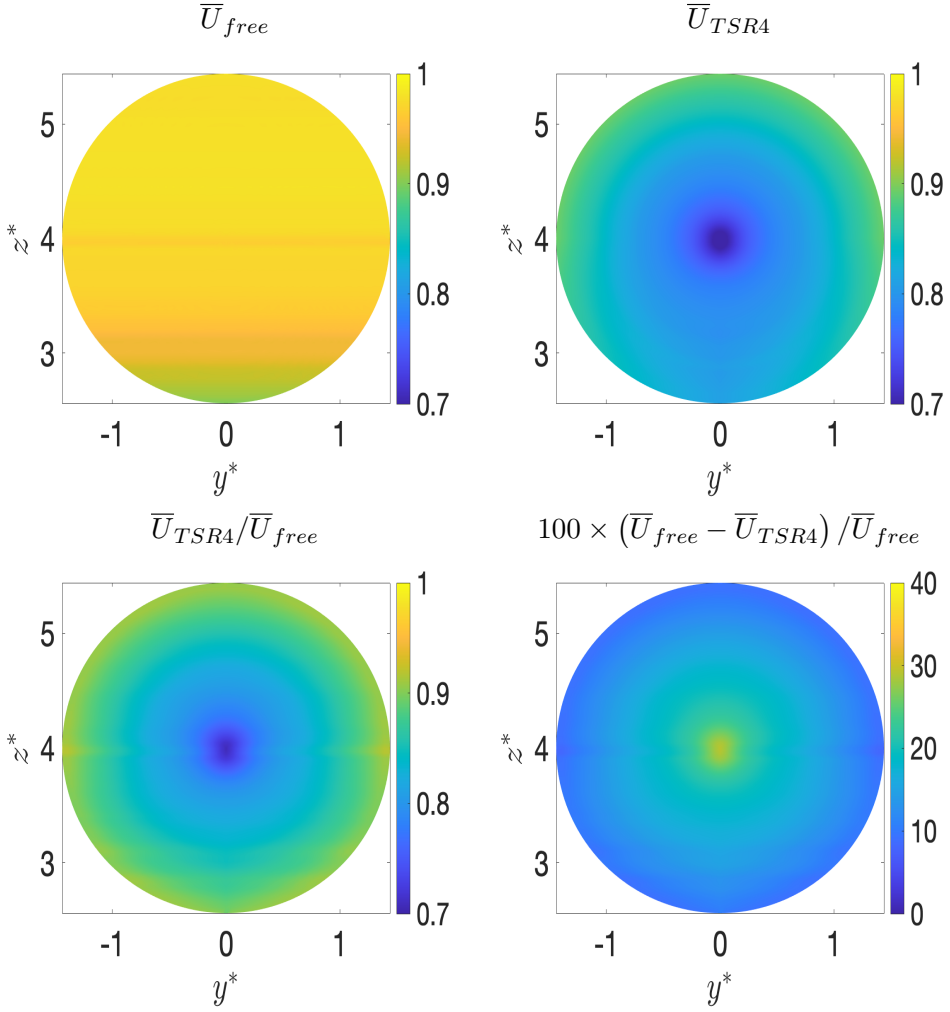

Figure 4: $C1C6$ flow configuration. Representation of the interpolated mean streamwise velocity component in the rotor (y, z) plane at $x^* = 16$. Top-Left: Free flow $\overline{U}_{free}$. Top-Right: In front of the turbine $\overline{U}_{TSR4}$. Bottom-left: Velocity ratio $\overline{U}_{TSR4}/\overline{U}_{free}$. Bottom-right: $100 \times \left(\overline{U}_{free} - \overline{U}_{TSR4}\right)/\overline{U}_{free}$.

point, TSR4. This confirms the main effect of the turbine rotational speed onto the mean flow deficit. For the present test-case, along the z-profile, the percentage deficit is accentuated by 2% when using $TSR = 5$ with regards of TSR4's results.

235 An estimation of the upstream axial deficit along the rotor axis can be provided from the analytical equation based on the axisymmetric vortex theory [39, 2]:

$$\overline{U}(x) = \overline{U}_{LDV}\left[1 - a\left(1 + \frac{x}{\sqrt{R^2 + x^2}}\right)\right] \tag{4}$$

where a is the axial induction factor, and x the axial coordinate. This analytical equation allows the determination of the values of $\overline{U}(x = -0.05)$ on the turbine axis that can be compared to the measured values (see table 2). An error be-

tween 1% and 14% is obtained, as a function of the streamwise position. These differences are directly linked to the reference velocity $\overline{U}_{LDV}$ used to compute the induction factor (see table 1), the associate velocity deficit and the limitation on the use of this theoretical equation in the nearest area of the turbine.

The axial mean free flow is homogeneous along the y direction across the rotor area [37]. For free case, a two-dimensional $(y-z)$ reconstruction of the mean flow can be then directly obtained from the vertical line measurement. An illustration is given in figure 4 (top-left) at $x^* = 16$. For the TSR4 case, the presence of the hub breaks the y-homogeneity. However, for an incoming uniform mean flow field, the mean velocity deficit is expected to be axisymmetric in front of the turbine. Thus, knowing that $\overline{U}_{free}(z^* = 4)$ is similar to $\overline{U}_{free}(z^* = 5.5)$ (see figure 3-left), one can expect that along the lines $z^* = 0, y \in [-R : R]$, $\overline{U}_{TSR4}$ values are similar to the ones along the line $y^* = 0, z \in [0 : R]$. Based on these assumptions, a two-dimensional reconstruction of the mean velocity field in the (r, θ)-plane at $x^* = 16$ is done by duplicating the mean values for each r and for $\theta \in [0 : \pi]$ and by performing a linear interpolation along r for $\theta = [\pi : 3\pi/2]$ and for $\theta = [3\pi/2 : 2\pi]$, to take into account the incoming mean shear flow. The resulted interpolated mean flow field is represented in figure 4 (top-right). Using a similar colormap, such a representation emphasizes the great disparities of both mean flow fields, especially in front of the hub and the blades. In this figure, the normalized velocities $\overline{U}_{TSR4}/\overline{U}_{free}$ as well as $100 \times \left(\overline{U}_{free} - \overline{U}_{TSR4}\right)/\overline{U}_{free}$ are also represented. The velocity deficit is found to be a function of the radial distance from the rotor-axis and it seems to be complicated to properly estimate this velocity deficit from a simplified one-dimensional model applied along the rotor axis. A quasi-uniform constant mean flow or a mean low shear flow approaching an operating turbine turns into a mean shear profile along the radial direction from the hub.

The thrust and power coefficients (equation 1) are now computed from the spatial average over the rotor area for the free and TSR4 cases, $\langle U_{free} \rangle$ and $\langle U_{TSR4} \rangle$ respectively (see table 3). These coefficients are compared (expressed in percentage values) to reference coefficients computed from $\overline{U}_{LDV}$ (see table 1). When using $\langle U_{free} \rangle$ as reference velocity, some great differences (between 13% and 34%, at $x^* = 10,\ 16,\ 23$) are observed by comparison with reference values. This emphasizes that upstream mean velocity measured at one point is not fully representative of the true free flow that impacts the turbine, especially when the flow is non-homogeneous. When using $\langle U_{TSR4} \rangle$, the values of the associated coefficients can not be realistic due to their own definition. This velocity $\langle U_{TSR4} \rangle$ has to be mainly related to the following characteristic velocity proposed in [51]:

$$u_T = \sqrt{\frac{\overline{T}}{\rho \pi R^2}} \tag{5}$$

The u_T values are also provided in the table 3. These values are always slightly smaller than $\langle U_{TSR4} \rangle$'s ones, suggesting that this characteristic velocity may not fully also representative of the mean velocity deficit in front of a turbine.

	C1C6			
	4	10	16	23
$\overline{U}_{TSR4}(x=-0.05)$	0.73	0.70	0.68	0.67
$\overline{U}(x=-0.05)$ (eq. 4)	0.62 (14%)	0.71 (1%)	0.70 (2%)	0.59 (11%)

Table 2: C1C6 flow configuration. Comparison of the mean streamwise velocity measurements in front of the turbine $\overline{U}_{TSR4}(x=-0.05)$ and its value based on analytical theory (equation 3) $\overline{U}(x=-0.05)$. The percentage values indicate the differences from both values.

	C1C6			
	4	10	16	23
$\langle U_{free} \rangle$	1.04 (1%)	0.97 (9%)	0.97 (6%)	0.95 (6%)
C_p	0.45 (3%)	0.50 (34%)	0.50 (20%)	0.51 (20%)
C_T	0.94 (2%)	1.01 (22%)	1.01 (13%)	1.05 (16%)
$\langle U_{TSR4} \rangle$	0.83 (20%)	0.80 (25%)	0.80 (22%)	0.78 (22%)
C_p	0.88 (102%)	0.89 (139%)	0.89 (113%)	0.92 (117%)
C_T	1.47 (60%)	1.49 (79%)	1.49 (66%)	1.52 (67%)
u_T	0.71	0.69	0.69	0.68

Table 3: C1C6 flow configuration. Comparison of the thrust and power coefficients in each x-section based on the spatial average over the rotor area for free and TSR4 cases, $\langle U_{free} \rangle$ and $\langle U_{TSR4} \rangle$ respectively. The percentage values indicate the differences from the reference coefficients computed from $\overline{U}_{LDV}$ (see table 1). Values of u_T (equation 5) are also indicated.

Figure 5 compares the mean vertical component $\overline{W}$, at the four turbine locations with and without turbine. $\overline{W}_{free}$ are represented as dashed lines and solid lines correspond to $\overline{W}_{TSR4}$. The normalized velocities, $100\times \mid \overline{W}_{free}(z) - \overline{W}_{TSR4}(z) \mid /\overline{U}_{free}(z)$ are also represented in this figure. $\overline{W}_{free}$ component approaches zero value along the vertical rotor diameter. In each x-section, the presence of the turbine leads to greatly modify the mean vertical component, $\overline{W}_{TSR4}$. The maximum magnitude of $\overline{W}_{TSR4}$ occurs near the edge of the rotor, with strong positive and negative values near the top and bottom of the rotor, respectively. This is in agreement with previous PIV measurements [39, 2] or Lidar and SPIV measurements [45, 33]. Medici et al. [39] showed that the radial mean velocity component upstream of the rotor in the horizontal center-turbine plane exhibits a peak value at 93% of the rotor radius marking the formation of the tip vortex. Similarly, one observes a peak value at 90% of the rotor radius for the $\overline{W}_{TSR4}$ component along the vertical line. This peak value is clearly identified in the upper part of the rotor at each section while it is less marked at the bottom. The highest absolute values of $\overline{W}_{TSR4}$ are between $0.08 - 0.2\text{m.s}^{-1}$ which correspond to $\sim 9.5\%$ of normalized velocities at the top turbine height and more than $16 - 18\%$ at the bottom (see figure 5-right). This shows that when normalized by the height-dependent mean streamwise velocities, the magnitudes of $\overline{W}_{TSR4}$ greatly differ near the rotor edges where most of the turbine power is generated. This asymmetric behavior was not noted in previous wind turbine studies, even if a mean slightly shear axial velocity profile in free flow was also present [45].

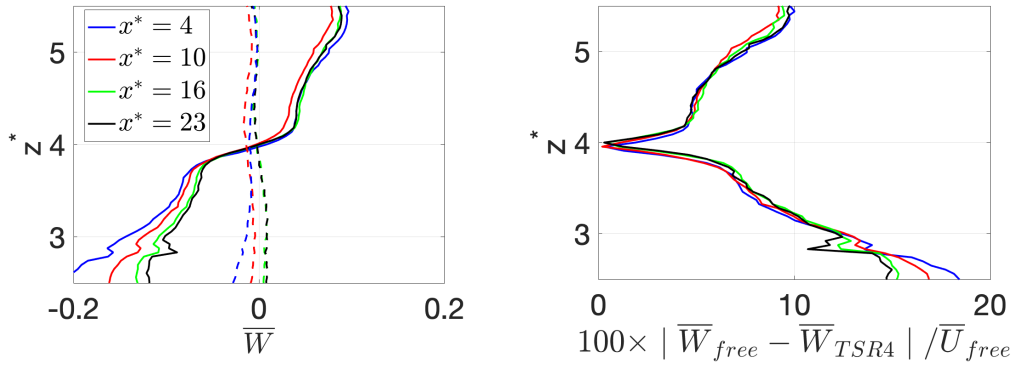

Figure 5: $C1C6$ flow configuration. Left: Superimposition of the vertical z-profiles of the mean vertical ($\overline{W}$) velocity component, for the four turbine locations: $x^* = 4$ (blue), $x^* = 10$ (red), $x^* = 16$ (green), $x^* = 10$ (black). The lines and dashed-lines correspond $\overline{W}_{TSR4}$ and $\overline{W}_{free}$ respectively. Right: Normalized velocities after subtracted from $\overline{W}_{TSR4}(z)$: $100\times \mid \overline{W}_{free}(z) - \overline{W}_{TSR4}(z) \mid /\overline{U}_{free}(z)$.

3.2. Turbine blockage effect on the Reynolds tensor components

After applying the Reynolds decomposition, the fluctuating velocity components are used to determine the associated normal Reynolds tensor components $\overline{u'^2}$ and $\overline{w'^2}$. Figure 6 compares both Reynolds tensor components computed in each streamwise section for free flow (dashed-lines) and in front of the turbine (solid lines). Even if the levels of $\overline{w'^2}_{free}$ are very small in the absence of the turbine, they seem to be not affected by the rotating turbine. Indeed, quasi similar $\overline{w'^2}$ profiles are observed in each section. $\overline{u'^2}$ profiles exhibit some slightly different behaviors. In the case of free flow, the velocity variance increases in the lower half ($z^* < 4$) at all locations, and the maximum at $x^* = 4$ is possibly due to pronounced curvature giving rise to the mean velocity gradient as can be seen in figure 3. The induction effect seems to reduce these variance values throughout the depth except at $x^* = 23$ where some similar levels remain. The normalized quantities $\overline{u'^2_{TSR4}}/\overline{u'^2_{free}}$ are also plotted in this figure (bottom-right). In each x-section, the maximum magnitude of $\overline{u'^2_{TSR4}}/\overline{u'^2_{free}}$ occurs in front of the hub, near twice for far downstream x-locations. This is due of the induced shear mean flow (due to the hub obstacle) discussed in the previous part, leading a locally increased level of $\overline{u'^2}_{TSR4}$.

4. Turbine induction effect in a turbulent shear flow

$C6$ flow configuration differs from previous one as Large Scale flow Structures (LSS) are self-organized in the water column to reach the free surface [28]. That allows the study of the induction effects in a more complex turbulent shear flow containing large scale flow structures. An analysis of the turbine blockage effect is successively done for the following quantities: mean velocity components, Reynolds tensor components, velocity spectra, two-point spatial velocity correlation, integral time scale and intermittency.

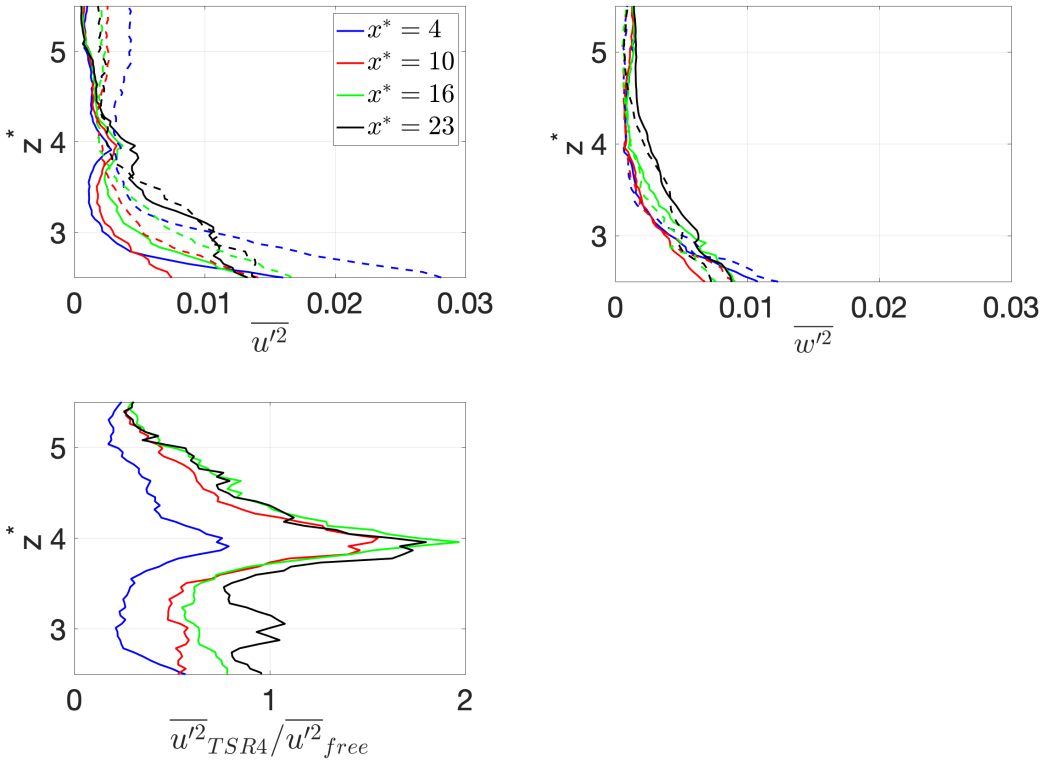

Figure 6: $C1C6$ flow configuration. Top-Left: Superimposition of the vertical profiles of the Reynolds components $\overline{u'^2_{TSR4}}$ (solid lines) and $\overline{u'^2_{free}}$ (dashed lines). Top-Right: Superimposition of the vertical profiles of the Reynolds components $\overline{w'^2_{TSR4}}$ (solid lines) and $\overline{w'^2_{free}}$ (dashed lines). Bottom: Normalized quantities $\overline{u'^2_{TSR4}}/\overline{u'^2_{free}}$.

4.1. Turbine blockage effect on the mean velocity components

Figure 7 compares the mean axial velocity component obtained in each x-section with and without turbine. The power laws (see equation 2) that best fit the velocity profiles are also indicated at $x^* = 16,\ 23$. At $x^* = 23$, the α exponent is in the range of the Alderney Race's values [44], that allows to mimic the in-situ conditions.

At $x^* = 4$, the results are quite similar to those presented for $C1C6$ flow configuration as $\overline{U}_{free}$ exhibits the same flow characteristics as $C1C6$ ones. As LSS grow in the far downstream field, shear $\overline{U}_{free}(z)$ profiles cover more and more the vertical extent of the rotor diameter. In the presence of the turbine, a velocity deficit is always found all along the measurement line with the highest deficit observed in front of the hub. At $x^* = 10$, the main vertical shear (observed in free flow) is globally well recovered while taking into account the velocity deficit due to the hub-obstacle and rotating blades.

A 2D reconstruction of the mean velocity is done similarly as the one described in §3.1. The thrust and power coefficients are determined using the spatial average over the rotor area for the free and TSR4 cases, $\langle U_{free} \rangle$ and $\langle U_{TSR4} \rangle$ respectively (see table 4). These coefficients are compared (expressed in percentage values) to

	C6			
	4	10	16	23
$\langle U_{free} \rangle$	1.07 (7%)	0.96 (11%)	0.90 (12%)	0.94 (3%)
C_p	0.43 (18%)	0.51 (46%)	0.53 (50%)	0.44 (10%)
C_T	0.90 (13%)	1.02 (29%)	1.04 (28%)	0.96 (6%)
$\langle U_{TSR4} \rangle$	0.87 (13%)	0.81 (25%)	0.74 (28%)	0.77 (21%)
C_p	0.81 (52%)	0.85 (144%)	0.96 (170%)	0.81 (100%)
C_T	1.36 (32%)	1.44 (81%)	1.58 (94%)	1.43 (59%)
u_T	0.72	0.69	0.66	0.65

Table 4: C6 flow configuration. Comparison of the thrust and power coefficients in each x-section based on the spatial average over the rotor area for free and TSR4 cases, $\langle U_{free} \rangle$ and $\langle U_{TSR4} \rangle$ respectively. The percentage values indicate the differences from the reference coefficients computed from $\overline{U}_{LDV}$ (see table 1). Values of u_T (equation 5) are also indicated.

reference coefficients computed from $\overline{U}_{LDV}$ (see table 1). As a function of the x-section, $\overline{U}_{LDV}$ values are higher, similar or smaller than $\langle U_{free} \rangle$. Consequently, the thrust and power coefficients differ to the reference ones up to 50% when using $\langle U_{free} \rangle$. This is a direct consequence of the vertical motion of the flow (see figure 2). In such an ascendent flow, usual velocity measurements performed $2D$ upstream of the turbine may be not representative (even at the first order statistics) of the flow impacting the turbine. This result may have potential consequences on the turbine power estimation based on classical reference mean velocity.
As stated previously, the calculation of these coefficients using $\langle U_{TSR4} \rangle$ is not realistic using classical formulations. When comparing $\langle U_{TSR4} \rangle$ values to characteristic velocity, u_T's ones (see equation 5), differences between 12% and 20% are obtained as a function of x-section. This confirms the difficulty in properly characterizing the mean flow deficit which greatly depends on the nature of incoming flow.

To further analyze the mean velocity deficit, the normalized velocities (see equation 3) are presented in figure 8. By comparison with previous results (figure 3), the ratio $\overline{U}_{TSR4}(z)/\overline{U}_{free}(z)$ exhibits some similarities whatever the x-section is. The maximum velocity deficit in front of the hub varies from 22% to 27%. At the rotor tip region, a velocity deficit between 7% and 12% is obtained which is in a good agreement with previous measurements in front of a wind turbine [45]. Globally, the mean flow deficit is around 15% for the last 25% of the blade length. The velocity profile is not symmetric as the one observed in the $C1C6$ wake configuration. The shear asymmetry is mainly observed at $x^* = 10$ and $x^* = 16$, and it is possibly due to the free vertical shear flow accentuated by the asymmetric effect due to the blade rotation as suggested by Bastankhah and Porte-Agel [2].

Analytical calculation of the velocity deficit is done using equation 4 (see Table 5). Great disparities appear at sections $x^* = 16$ while a good agreement is obtained for both other sections. Note that previous similar differences have been noted [39, 45] and at the same time, a good agreement between analytical formulae

results and experimental measurements was already presented [2, 47]. This result emphasizes that not only one-dimensional simplified model for velocity deficit determination may be questionable in present flow configuration but certainly also the determination of the induction factor a which is based on $\overline{U}_{LDV}$ measurements 2D upstream the turbine, in the present study.

Finally, by comparison with the free mean flow, the mean streamwise velocity component is greatly modified in front of the turbine and the (smooth or high) vertical mean flow profile as well as its repartition across the rotor has an influence on the modification of the velocity deficit observed in front of the turbine.

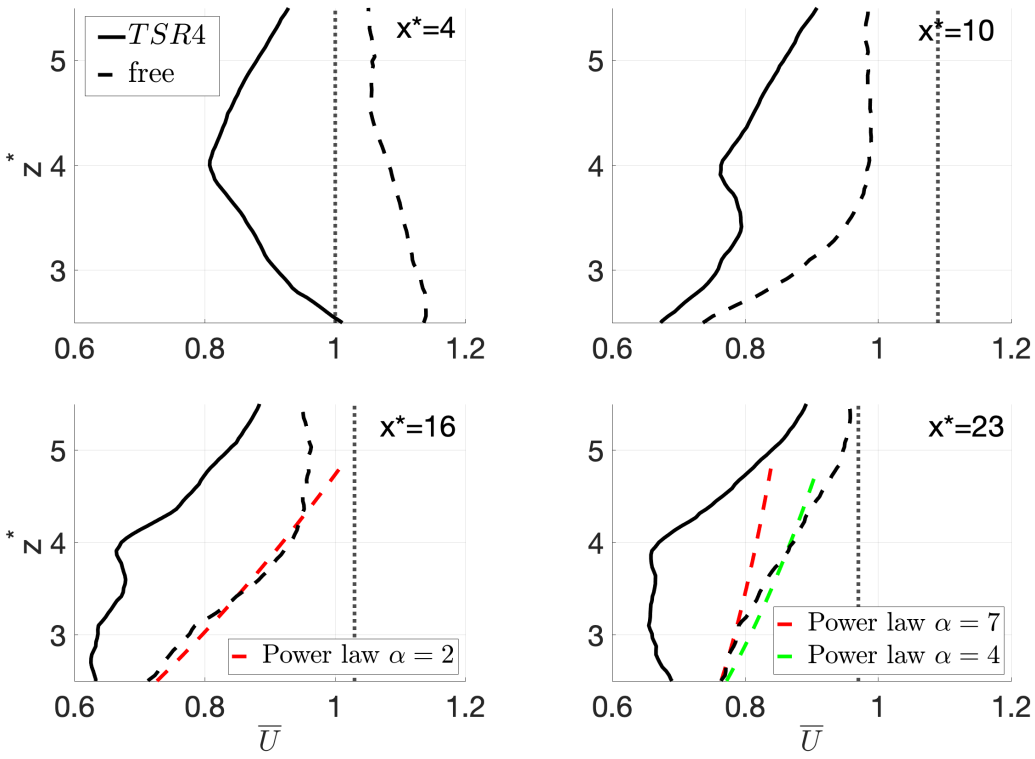

Figure 7: $C6$ flow configuration. Superimposition of the vertical profiles of the mean streamwise velocity component $\overline{U}$ for the four turbine locations: $x^* = 4$ (top-left), $x^* = 10$ (top-right), $x^* = 16$ (bottom-left), $x^* = 23$ (bottom-right). $\overline{U}_{TSR4}$ (solid lines), $\overline{U}_{free}$ (dashed lines) and dotted lines correspond to one-point LDV measurements, $\overline{U}_{LDV}$ at $z^* = 4$, and duplicated over the rotor diameter. Power law velocity profiles are also indicated at $x^* = 16, 23$.

Figure 9 compares the evolution of the vertical mean velocity component $\overline{W}_{free}$ and $\overline{W}_{TSR4}$ along the rotor diameter. The normalized velocities are also plotted for analysis. Without turbine, $\overline{W}_{free}$ component exhibits a quasi-null value all along the vertical measurement line. The turbine induces a modification of the $\overline{W}_{TSR4}$ profiles: a vertical shear is observed with positive value above hub height and negative values below hub height. Highest absolute values of $\overline{W}_{TSR4}$ are obtained near the rotor edges, of an order of $0.1 - 0.13\text{m.s}^{-1}$. These values seem to be not negligible compared to those of $\overline{U}_{TSR4}$. They correspond to more than

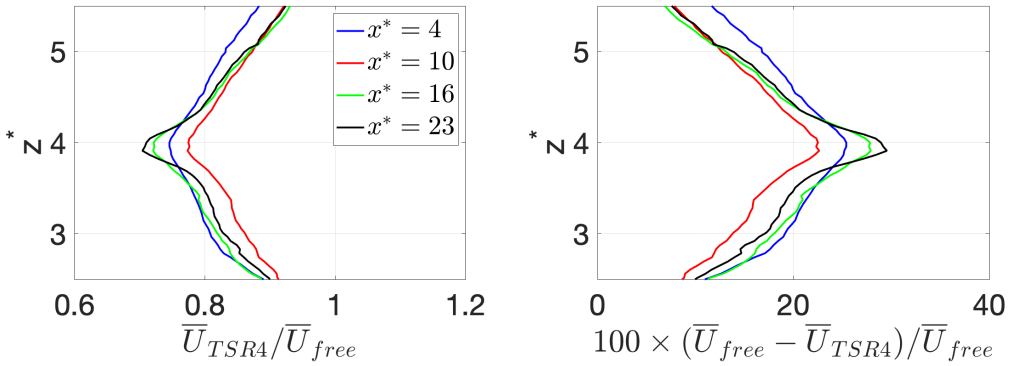

Figure 8: $C6$ flow configuration. Superimposition of the normalized velocities: $\overline{U}_{TSR4}(z)/\overline{U}_{free}(z)$ (left) and $100\times \mid \overline{U}_{free}(z) - \overline{U}_{TSR4}(z) \mid /\overline{U}_{free}(z)$.

	C6			
	4	10	16	23
$\overline{U}_{TSR4}(x=-0.05)$	0.81	0.76	0.66	0.66
$\overline{U}_{x=-0.05}$ (eq. 4)	-	0.75 (1%)	0.80 (21%)	0.72 (9%)

Table 5: C6 flow configuration. Comparison of the mean streamwise velocity measurements in front of the turbine $\overline{U}_{TSR4}(x=-0.05)$ and its value based on analytical theory (equation 4) $\overline{U}(x=-0.05)$. The percentage values indicate the differences from both values. At $x^* = 4$, $\overline{U}_{x=-0.05}$ can not be determined as $C_T > 1$ (table 1).

18% of the mean streamwise component at the bottom of the rotor and more than 8% at the top position. The peak values are obtained at 90-95% of the rotor radius, which is similar to previous study [39]. As previously observed in $C1C6$ flow configuration, an asymmetric $\overline{W}_{TSR4}$ profile is obtained with the highest shear vertical profile below the hub height where the mean streamwise velocity component exhibits its highest shear.

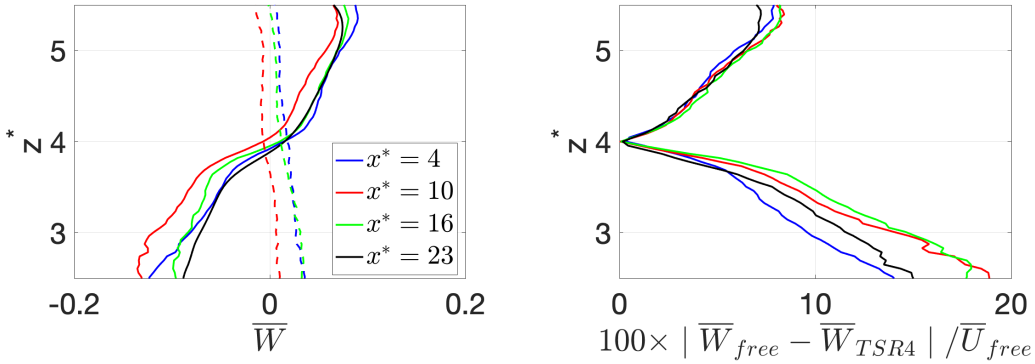

Figure 9: $C6$ flow configuration. Left: Superimposition of the vertical profiles of the mean vertical velocity component $\overline{W}_{TSR4}$ (solid lines) and $\overline{W}_{free}$ (dashed lines) for the four turbine locations: $x^* = 4$ (blue), $x^* = 10$ (red), $x^* = 16$ (green), $x^* = 10$ (black). Right: Normalized velocities after subtracted from $\overline{W}_{TSR4}(z)$: $100\times \mid \overline{W}_{free}(z) - \overline{W}_{TSR4}(z) \mid /\overline{U}_{free}(z)$.

4.2. Turbine blockage effect on the Reynolds tensor components

Figure 10 presents the Reynolds tensor components $\overline{u'^2}$ and $\overline{w'^2}$. Even if the $C6$ wake flow is slightly more turbulent than $C1C6$ flow configuration, some similar conclusions can be drawn. In each x-section, $\overline{u'^2}$ and $\overline{w'^2}$ remain globally unchanged in front of the turbine by comparison with the free flow.

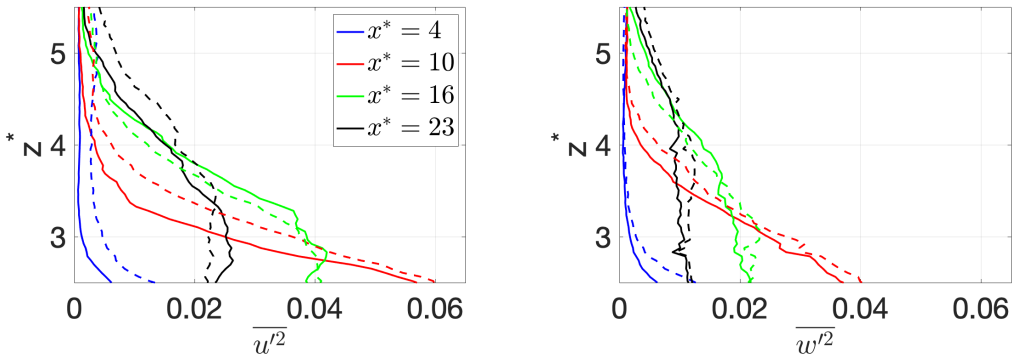

Figure 10: $C6$ flow configuration. Left: Superimposition of the normalized Reynolds components $\overline{u'^2}_{TSR4}$ (solid lines) and $\overline{u'^2}_{free}$ (dashed-lines) along the vertical rotor diameter. Right: Superimposition of the normalized Reynolds components $\overline{w'^2}_{TSR4}$ (solid lines) and $\overline{w'^2}_{free}$ (dashed-lines).

4.3. Spectral analysis of the flow in front of the turbine

In this $C6$ flow configuration, it was recently demonstrated that Large Scale periodic flow Structures (LSS) associated with a low frequency signature are responsible of the main turbine power fluctuations [15]. In order to investigate the induction effect on these LSS, a Fourier analysis is conducted in each section from instantaneous fluctuating (u', w') velocity components measured in front of the turbine and in the free flow. The Discrete Fourier Transform is applied to the fluctuating velocity signal which is splitted into blocks of 1024 samples with an overlapping of 50%. The velocity spectrum is then averaged over blocks and a smoothing technique is finally applied to it. Figure 11 represents the u'-spectra expressed as frequency and computed at three selected z-positions: $z_1^* = 3$, $z_2^* = 4$ and $z_3^* = 5$ for TSR4 (solid lines) and free (dotted lines) cases and at each streamwise position. Note that z_2^* corresponds exactly to the hub center position. The w'-spectra (not shown) exhibit similar characteristics as u'-spectra, though the amplitudes are relatively smaller. In the free flow, at $x^* = 4$, whatever the z location, the flow is quasi-uniform and no frequency peaks emerge [15]. Far downstream, $x^* > 10$, the low frequency passage of the LSS is very well marked and the rising of these structures is clearly indicated by the frequency peak extension over z^*. At $x^* = 23$, the peak values cover the largest z domain, it is still visible at each z_1^*, z_2^* and z_3^*. When regarding the velocity spectra determined in front of the turbine, they show broad similarities with velocity spectra in free flow. Small differences between both spectral representations can be observed at $x^* = 23$. Indeed, the frequency peak associated with LSS is not marked in front of

the hub ($z^* = 3$). This difference can be attributed to the hub obstacle effect that modifies locally the flow dynamics, knowing that at TSR4 the induction effect are sensitive up to 1D upstream the rotor plane [11].

This spectral analysis demonstrates that the low frequency signature of the LSS is not affected in front of the rotating blades, but it is still slightly modified in front of the hub obstacle. To the author knowledge, similar measurements with and without turbine have never been previously performed, avoiding any well comparison with previous analyses. Previous analytical and numerical investigations based on Rapid Distortion Theory concluded that the magnitude of the large scale structures can be amplified [21, 38] while a recent study seems to lead to an attenuation of the large scale structure's fluctuations [41]. Moreover, numerical simulations based on vortex particle method [6] showed that the presence of the wind turbine does not affect the turbulence spectrum significantly. Previous cited works are based on assumptions that are not satisfied in the present flow configurations. Furthermore, a recent work showed that upstream turbulence spectrum modifications are greatly dependent of the turbine rotational speed and upstream turbulence integral length scale [11].

Note also that for each flow configuration (with and without turbine), each u'-spectrum follows a power law decay of $-5/3$ (black dashed line in figure 11) in the inertial range, demonstrating that the energy transfer mechanisms seems to be not affected by the turbine presence.

4.4. Analysis of the integral time scale and high-order statistics

The effect of turbine blockage is now examined from the statistical autocorrelation coefficient computed from each velocity component between two points (z_1, z_2). Equations 6 and 7 give the formulation of both R_u and R_w correlation coefficients:

$$R_u(z_1, z_2) = \frac{\overline{u'(z_1,t)u'(z_2,t)}}{\sqrt{\overline{u'(z_1,t)u'(z_1,t)}}\sqrt{\overline{u'(z_2,t)u'(z_2,t)}}} \tag{6}$$

$$R_w(z_1, z_2) = \frac{\overline{w'(z_1,t)w'(z_2,t)}}{\sqrt{\overline{w'(z_1,t)w'(z_1,t)}}\sqrt{\overline{w'(z_2,t)w'(z_2,t)}}} \tag{7}$$

As LSS are mainly present at $x^* = 16$ and $x^* = 23$, these two sections are only retained for the following analyses. Figure 12 represents isosurfaces of both R_u and R_w correlation coefficients computed at $x^* = 23$. We voluntary limit the colormap to $[0.5 : 1]$ to better underline the differences. The correlation decay is more marked than in the other $x^* = 16$ (not shown), especially around the hub center which corresponds to the LSS passage area in this section. To better appreciate these differences, figure 13 displays the correlation coefficients $R_u(z_1, z^*)$ and $R_w(z_1, z^*)$ computed at two selected points: $z_1^* = 3$ and $z_1^* = 4$ and expressed as a function of z^*. The spatial correlation for TSR4 case reduces rapidly for $z^* > 4$ compared to free case. This spatial correlation decrease comes from the hub effect which greatly affects the LSS in front of it. Around the hub ($z^* = 4$) and at $z^* = 3$, free velocity components are correlated over an

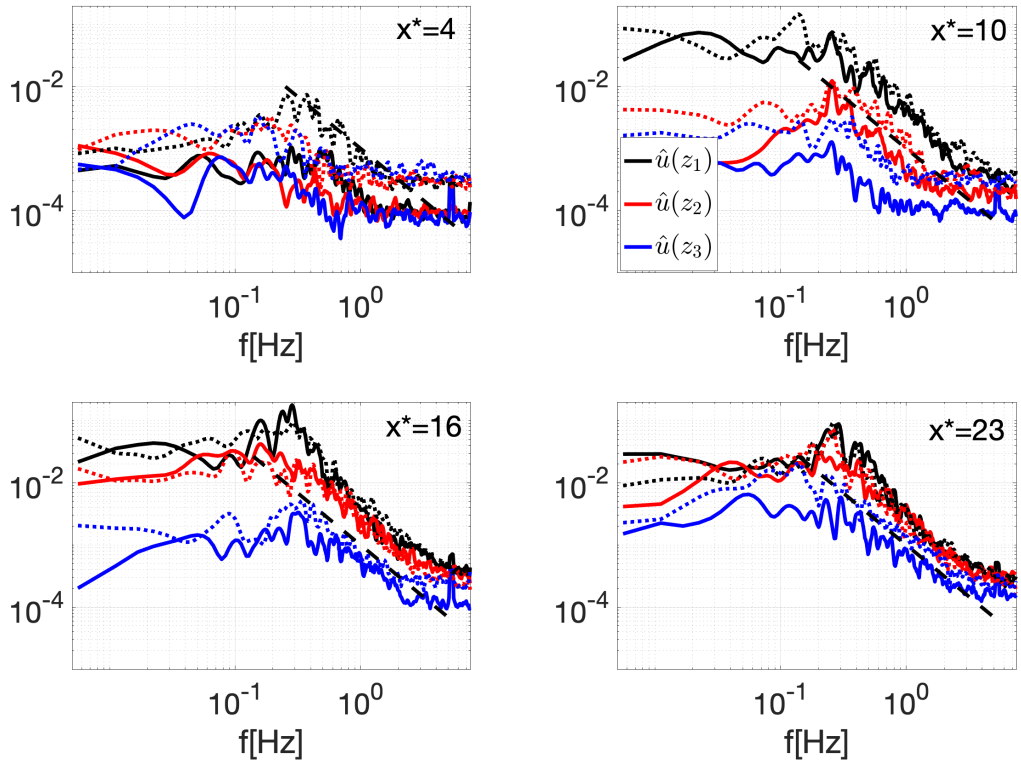

Figure 11: $C6$ flow configuration. u'-spectra computed at three selected z-positions: $z_1^* = 3$, $z_2^* = 4$ and $z_3^* = 5$ for TSR4 (solid lines) and free (dotted lines) cases. The black dashed line indicates the power law decay of $-5/3$.

higher vertical extent by comparison with the correlation computed upstream the turbine. This seems to indicate that the spatial correlation length is reduced in the presence of the rotor, especially due to the presence of the hub.

The integral time scales of the flow are now determined along the rotor diameter. For this, we apply the procedure detailed in [14]. Briefly, the temporal auto-correlation $R_u(z,\tau) = \overline{u'(z,t)u'(z,t+\tau)}$ is calculated at each z position along the vertical line. Then, one integrates the temporal correlation in time until it crosses zero for the first time to access the integral time scale, $T_u(z)$. Note that this scale is primarily due to the presence of LSS at the x-location. The evolution of the integral time scales along the z-line is displayed in figure 14. In the free flow, one recovers the maximal value of the integral time scale of 0.45s which corresponds to an integral length scale of 0.4m using the local Taylor hypothesis under frozen turbulence [14]. This maximal value is recovered around $z^* = 3.5$ at $x^* = 16$ and around $z^* = 4 - 4.5$ at $x^* = 23$ due to the rising motion of the flow structures. At $x^* = 16$, the integral time scales computed in front of the turbine exhibits a similar tendency over the z extent as the one in the free flow. When LSS moves below the hub height (section $x^* = 16$), the rotating blades do not greatly impact the flow organization. This result is in agreement with previous's ones when the blade load spectra exhibit some frequency peaks at the

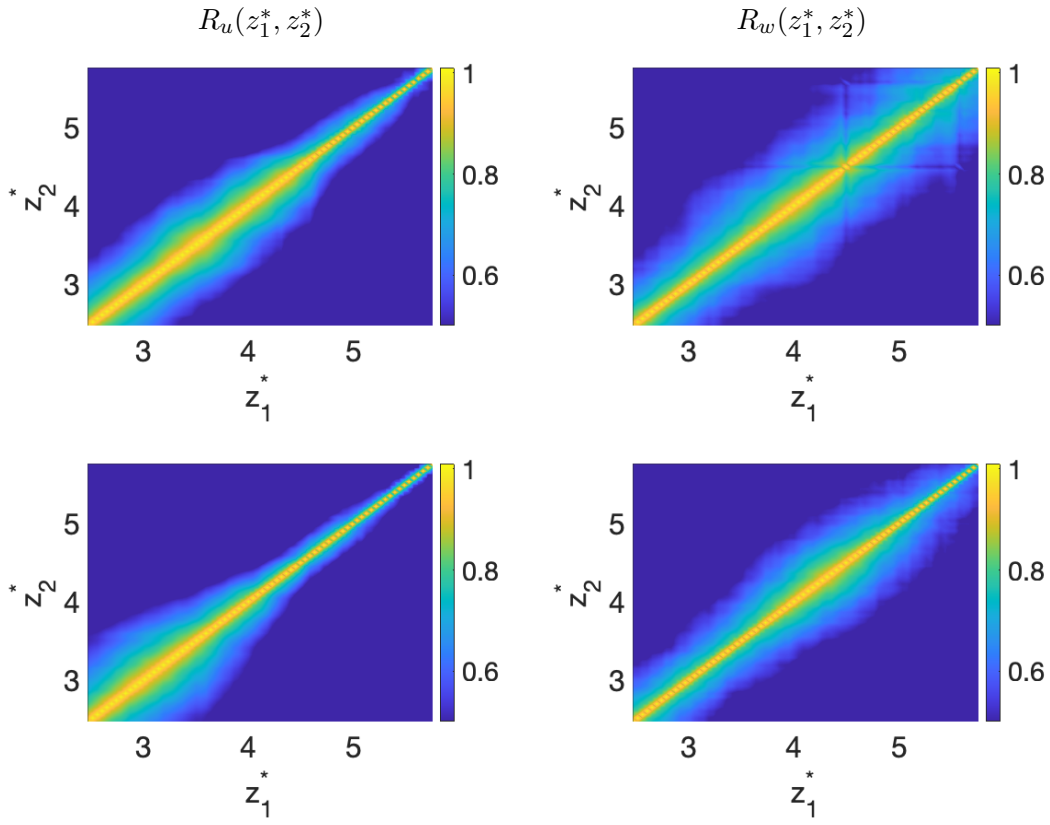

Figure 12: $C6$ flow configuration. $x^* = 23$ section. Representation of the two point correlation coefficients: $R_u(z_1^*, z_2^*)$ (left column) and $R_w(z_1^*, z_2^*)$ (right column) for free (top row) and TSR4 (bottom row) cases.

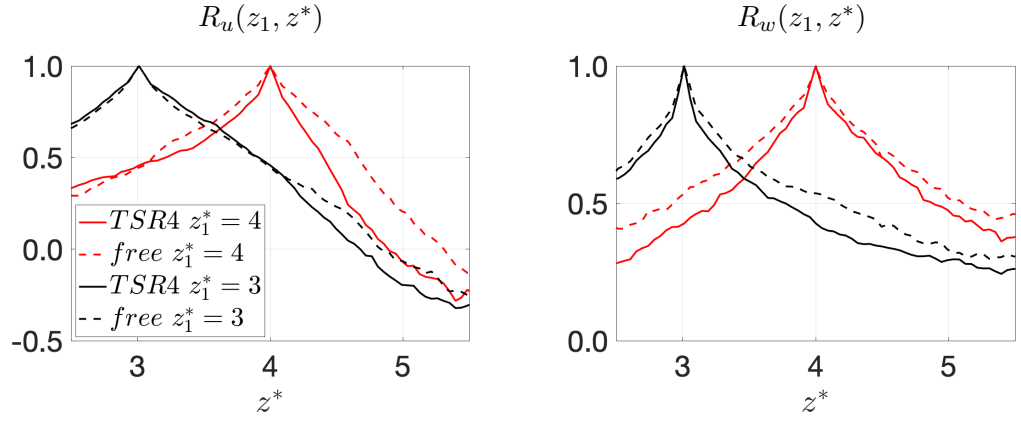

Figure 13: $C6$ flow configuration. $x^* = 23$ section. Left: Superimposition of $R_u(z_1, z^*)$ with $z_1^* = 3$ and $z_1^* = 4$ computed from free flow (dashed lines) and flow with turbine (solid lines) Right: Superimposition of $R_w(z_1, z^*)$ with $z_1^* = 3$ and $z_1^* = 4$ computed from free flow (dashed lines) and flow with turbine (solid lines).

frequency passage of the large scale structures [14, 15]. The main difference is

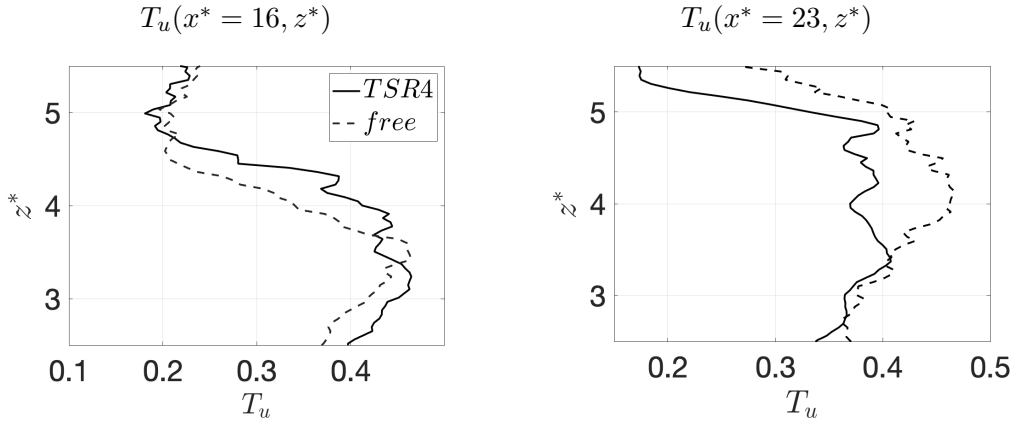

Figure 14: $C6$ flow configuration. $x^* = 16$ (left). $x^* = 23$ (right). Evolution of the integral time scales computed along the vertical line for TSR4 (solid lines) and free (dashed lines) cases.

observed in front of the hub where a reduction of 17% of the integral time scale is obtained. At $x^* = 23$, the modifications of the integral time scale are also mainly observed near the hub where the integral time scale is 20% smaller than the one in the free flow. This is due to the passage of LSS which mainly occurs at the hub region which leads to LSS break down and then affects the flow reorganization. However, the standard deviations of the turbine thrust for $x^* = 16$ and $x^* = 23$ were found to be of the same order of magnitude [15]. The integral length scale in the inflow (free flow) is of size 0.4m is nearly order of the turbine radius which after breakdown reorganizes possibly to higher frequency end. This could be then related to previous studies that scales beyond cut-off frequency will not play any significant role in power fluctuations [8, 11].

Globally, one expects that such LSS breakdown would be certainly different depending on the inflows and possibly the reorganization. Previous spectral analysis (§4.3) shows that the -5/3 power law decay is observed in the inertial range of the u'-spectrum in front of the turbine. This seems to confirm that the energy transfer mechanisms remains the same even in the presence of the turbine. Furthermore, some new analyzes have to be performed to further analyze the flow organization including the modifications of the small scale fluctuations and also the flow intermittency. To this end, some preliminary analyses are proposed in the following.

First, high order statistics as skewness S and flatness T coefficients related to the fluctuating streamwise velocity component:

$$S = \frac{\overline{u'^3}}{\overline{u'^2}^{3/2}} \quad \text{and} \quad T = \frac{\overline{u'^4}}{\overline{u'^2}^2} \tag{8}$$

are computed at each x-section. For Gaussian type PDF function, $S = 0$ and $T = 3$. Figure 15 displays these coefficients determined in the free-flow (dashed lines) and in TSR4 (solid lines) cases. At $x^* = 4$, as the free flow is uniform (for $z^* > 3$), one recovers the expected $S = 0$ and $T = 3$. Conversely, at this section,

in front of the turbine, the flow modifications break down this intermittency that leads to different skewness and flatness values. A modification of sign is observed for the skewness coefficient emphasizing a symmetry modification about the mean value. In the other sections, the LSS passage results in some most important changes of the skewness coefficient across the vertical z-line. As x^* increases, the smallest values of S move to the top following the motion of the LSS in the water column. This is also in agreement with the flatness representation showing peak values corresponding to the location of the LSS passage. It is interesting to observe that S and T coefficients exhibit a similar tendency whatever the flow configurations (free and TSR4). Based on these z-line measurements, it seems that the turbine does not affect significantly the flow intermittency, in the presence of a non-homogeneous incoming flow. However, the intermittency of incoming homogenous Gaussian fluctuations is more impacted by the turbine and increases in front of it. The incoming Gaussian fluctuations turn out to become non-Gaussian. Such a modification may have some consequences on the turbine load interpretations [3].

Second, as the main flow modifications in front of the turbine concerns the mean velocity profile, one proposes to examine the instantaneous velocity gradient $\partial u/\partial y$. This term represents one of the dominant term in the kinetic energy dissipation rate, which also plays a special role in the study of intermittency effect in turbulence. Figure 16 presents the resulting pdfs for each flow configuration (free and TSR4) at each streamwise position. Once again, the main difference between free and TSR4 cases is observed at $x^* = 4$, where the homogeneous $\overline{U}$ profile is the most impacted by the turbine presence. Far downstream in the presence of LSS, the resulted pdfs are quite similar in both the free and TSR4 cases. Some very small differences appear at the tails of the pdf.

Globally, the present flow measurements demonstrate that in the presence of an incoming non-homogeneous shear flow, the turbine presence does not greatly impact the flow intermittency. This constitutes some preliminary results and has to be confirmed with future measurements of the three velocity components in the whole three-dimensional induction region or with numerical simulations. Furthermore, a lot of parameters such as turbine rotational speed, incoming turbulence level, wavy environment, rotor yawed and others may certainly also influence these flow modifications and have to be future analyzed.

5. Summary and discussion

The turbine blockage effect, more commonly referred as turbine induction, was studied as a function of various turbulent flow conditions, including low and high mean velocity shear and complex flow dynamics with large-scale flow structures. When the incoming flow is a uniform contant or a low-shear mean axial velocity field with a low turbulence level, the flow modifications in front of a turbine are quite similar. Most of the mean axial velocity deficit ($\sim 30\%$) is observed in front of the hub obstacle while this velocity deficit is of an order of 10% at the rotor edge. The turbine's blockage induces two symmetric vertical shear axial velocity profiles above and below the hub height. While the mean vertical velocity com-

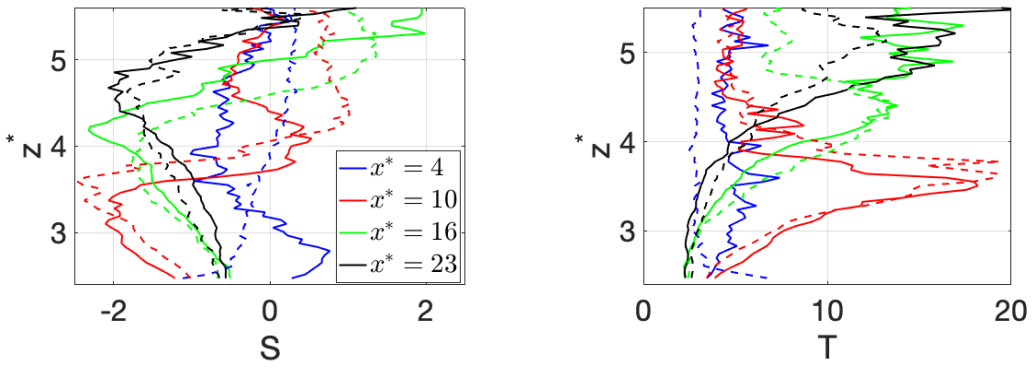

Figure 15: $C6$ flow configuration. Skewness (left) and flatness (right) coefficients related to the fluctuating streamwise velocity component, for TSR4 (solid lines) and free (dashed lines) cases.

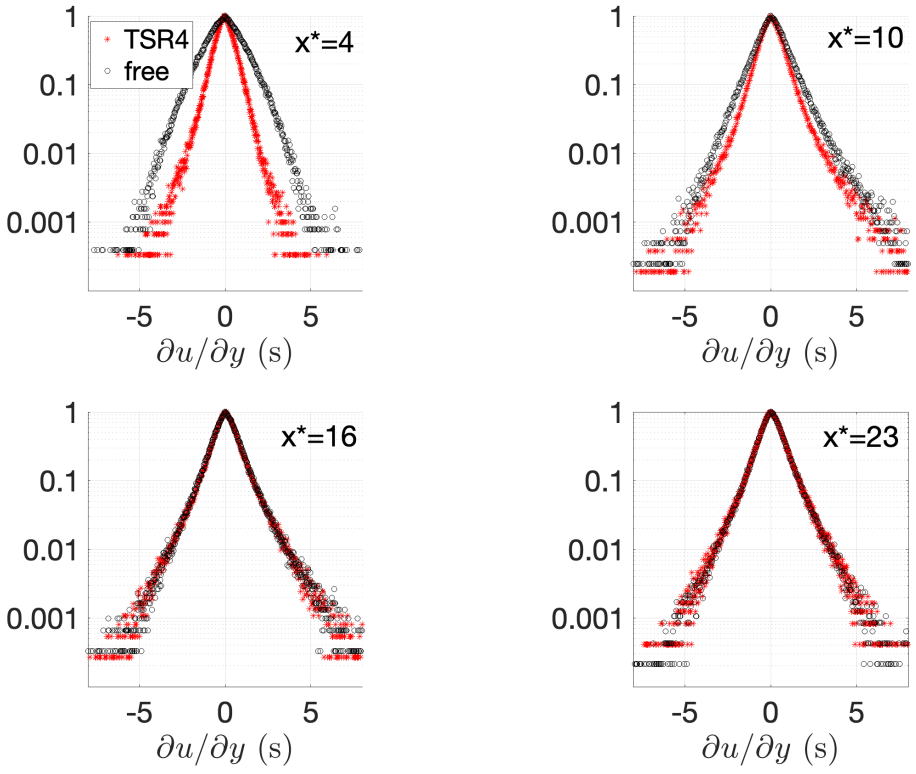

Figure 16: $C6$ flow configuration. PDF of the instantaneous velocity gradient $\partial u/\partial y$ for TSR4 (solid lines) and free (dashed lines) cases.

ponent approaches zero in the free flow, some positive induced $\overline{W}$ velocities are found above the hub height and negative induced ones below the hub height. The mean vertical velocity component exhibits its highest values near the blade edge where the tip vortex is initiated. In such an incoming homogenous Gaussian flow field, the main flow modifications in front of the turbine concern the intermittency. The turbine's blockage induces some turbulent non-Gaussian fluctuations.

When the turbine is subjected to a more complex turbulent flow including a more accentuated mean shear axial velocity profile and some large-scale flow structures rising in the water column, the mean axial velocity profile greatly differs from the one observed in free flow without turbine. The turbine's blockage effect is directly linked to the nature (low or high shear and its extension over the vertical rotor diameter) of the mean free incoming flow. The mean vertical velocity component exhibits an asymmetric shear profile along the vertical direction, with non-negligible positive and negative values above and below the hub height respectively. In front of the turbine, the Reynolds tensor components $\overline{u'^2}$ and $\overline{w'^2}$ are less impacted than the mean velocities. The low frequency large scale flow structures are mainly affected by the hub and less by the rotating blade's blockage effect. The flow organization is altered in front of the hub with a noticeable modification of the integral time scale.

Present work also demonstrates that in the presence of a complex incoming turbulent flow, a one-point (or even several points) measurements of a reference velocity, at two diameters upstream the turbine, are not always representative of the mean velocity impacting the turbine. Indeed, between this measurement point and the rotor, the flow could evolve in a different manner as it is the case here when LSS are rising in the wake of a surface-mounted obstacle, representative of a specific bathymetry. In such a complex flow configuration, a background correction has to be applied to the mean reference velocity measurements before applying velocity deficit model or using it as reference velocity for the turbine performance computations.

On the other hand, the theoretical one-dimensional velocity deficit model used when the turbine rotor is viewed as an actuator disk or line may be questionable to accurately represent the upstream flow-turbine interactions. It is then expected that present experimental database provides useful data information allowing to improve and validate future velocity deficit models used in upstream turbine's induction region and also to improve the understanding of the relationship between turbine and incoming turbulent flow.

Finally, some potential topics of further research are proposed.

First, the turbulence second-order statistics ($\overline{u'^2}$ and $\overline{w'^2}$) are found to be not affected by the turbine's blockage effect along the vertical rotor diameter. New experiments have to be carried out to state about the possible modifications of the turbulent kinetic energy in front of the turbine. The characterization of the turbulent kinetic energy budget would be desirable to fully complete the turbulence characterization within the induction region. Such an investigation needs the measurements of the three velocity components in the whole induction region.

Second, it will also be important to extend analyses by considering the influence

of the turbine rotational speed, the wavy environment, the incoming turbulence level and the yaw misalignment onto the turbine's blockage flow effect.
Third, as recently observed from numerical simulations of offshore floating wind turbines [34], incoming wind shear turbulence has a limited impact on the rotor performance, but a noticeable influence on the blade fatigue. Consequently, as the flow organization is found to be altered in front of a tidal turbine, the relationship between these modifications and the blade structural fatigue should be addressed.

Acknowledgements

This research was partly funded by the Region Hauts-de-France in the framework of the project CPER 2015-2020 MARCO. The authors would like to gratefully acknowledge Maria Ikhennicheu and Benoît Gaurier involved in the experimental database generation and to warmly thank Thomas Bacchetti and Jean-Valery Facq for their assistance and precious advices.
The authors also gratefully acknowledge the contribution from the anonymous reviewers. Their insightful comments and meaningful suggestions helped us improve the quality of the present study.

CRediT authorship contribution statement

Philippe Druault: Data analysis, software, formal analysis, writing-original draft, review and editing. **Grégory Germain**: Conceptualization, Methodology, Funding acquisition, writing- review and editing.

References

References

[1] Bahaj, A.S., Molland, A.F., Chaplin, J.R., Batten, W.M.J., 2007. Power and thrust measurements of marine current turbines under various hydrodynamic flow conditions in a cavitation tunnel and a towing tank. Renew. Energy 32, 407–426.

[2] Bastankhah, M., Porte-Agel, F., 2017. Wind tunnel study of the wind turbine interaction with a boundary-layer flow: Upwind region, turbine performance, and wake region. Phys. Fluids 29, 065105.

[3] Berg, J., Natarajan, A., Mann, J., Patton, E., 2016. Gaussian vs non-gaussian turbulence: impact on wind turbine loads. Wind Energy 19, 1975–1989.

[4] Blackmore, T., Myers, L., Bahaj, A., 2016a. Effects of turbulence on tidal turbines: Implications to performance, blade loads and condition monitoring. Int. J. Mar. Energy 14, 1–26.

[5] Blackmore, T., Myers, L., Bahaj, A., 2016b. Effects of turbulence on tidal turbines: Implications to performance, blade loads and condition monitoring. Int. J. Mar. Energy 14, 1–26.

[6] Branlard, E., Mercier, P., Machefaux, E., Gaunaa, M., Voutsinas, S., 2016. Impact of a wind turbine on turbulence: Un-freezing turbulence by means of a simple vortex particle approach. J. Wind Eng. Ind. Aerodynamics 151, 37–47.

[7] Branlard, E., Meyer Forsting, A., 2020. Assessing the blockage effect of wind turbines and wind farms using an analytical vortex model. Wind Energy 23, 2068–2086.

[8] Chamorro, L.P., Hill, C., Morton, S., Ellis, C., Arndt, R.E.A., Sotiropoulos, F., 2013. On the interaction between a turbulent open channel flow and an axial-flow turbine. J. Fluid Mech. 716, 658–670.

[9] Choma Bex, C., Carlier, C., Fur, A., Pinon, G., Germain, G., Rivoalen, É., 2020. A stochastic method to account for the ambient turbulence in lagrangian vortex computations. Applied Mathematical Modelling 88, 38–54.

[10] Conway, J.T., 1995. Analytical solutions for the actuator disk with variable radial distribution of load. J. Fluid Mech. 297, 327–355. f

[11] Deskos, G., Payne, G.S., Gaurier, B., Graham, M., 2020. On the spectral behaviour of the turbulence-driven power fluctuations of horizontal-axis turbines. J. Fluid Mech. 904, A13.

[12] Dimitrov, N., Borraccino, A., Pente, A., Mann, J., 2019. Wind turbine load validation using lidar-based wind retrievals. Wind Energy 22, 1512–1533.

[13] Dose, B., Rahimi, H., Herr, I., Stoevesandt, B., Peinke, J., 2018. Fluid-structure coupled computations of the nrel 5mw wind turbine by means of cfd. Renew. Energy 129, 591–605.

[14] Druault, Ph., Gaurier, B., Germain, G., 2022. Spatial integration effect on velocity spectrum: Towards an interpretation of the $-11/3$ power law observed in the spectra of turbine outputs. Renew. Energy 181, 1062–1080.

[15] Druault, Ph., Germain, G., 2022. Prediction of the tidal turbine power fluctuations from the knowledge of incoming flow structures. Ocean Eng. 252, 111180.

[16] Gambuzza, S., Ganapathisubramani, B., 2021. The effects of free-stream turbulence on the performance of a model wind turbine. J. Renew. Sustainable Energy 13, 023304.

[17] Gaurier, B., Druault, Ph., Ikhennicheu, M., Germain, G., 2020a. Experimental analysis of the shear flow effect on tidal turbine blade root force from three-dimensional mean flow reconstruction. Phil. Trans. R. Soc. A 378 20200001.

[18] Gaurier, B., Germain, G., Pinon, G., 2019. How to correctly measure turbulent upstream flow for marine current turbine performances evaluation?, in: Advances in Renewable Energies Offshore - Proceedings of the 3rd International Conference on Renewable Energies Offshore, RENEW 2018, pp. 23–30.

[19] Gaurier, B., Ikhennicheu, M., Germain, G., Druault, Ph., 2020b. Experimental study of bathymetry generated turbulence on tidal turbine behaviour. Renew. Energy 156, 1158–1170.

[20] Gaurier, B., Ordonez-Sanchez, S., Facq, J.v., Germain, G., Johnstone, C., Martinez, R., Salvatore, F., Santic, I., Davey, T., Old, C., Sellar, B., 2020c. MaRINET2 Tidal Energy Round Robin Tests-Performance Comparison of a Horizontal Axis Turbine Subjected to Combined Wave and Current Conditions. J. Marine Sc. Eng. 8, 463.

[21] Graham, J.M., 2017. Rapid distortion of turbulence into an open turbine rotor. J. Fluid Mech. 825, 764–794.

[22] Howard, K., Chamorro, L., Guala, M., 2016. A comparative analysis on the response of a wind-turbine model to atmospheric and terrain effects. Boundary Layer Meteo. 158, 229–255.

[23] Howard, K., Guala, M., 2015. Upwind preview to a horizontal axis wind turbine: a wind tunnel and field-scale study. Wind Energy 19, 1371–1389.

[24] IEC, 2013. Marine energy - Wave, tidal and other water current converters - Part 200: Electricity producing tidal energy converters - Power performance assessment. Technical Report, International Electrotechnical Commission, Geneva, Switzerland.

[25] IEC, 2017. Wind Turbine Generator Systems–Part 12-2 : Power Performance of Electricity-Producing Wind Turbines Based on Nacelle Anemometry. Technical Report, 61400-12-2:2017.

[26] Ikhennicheu, M., 2019. Étude expérimentale de la turbulence dans les zones à forts courants et de son impact sur les hydroliennes. Ph.D. thesis. Université de Lille.

[27] Ikhennicheu, M., Germain, G., Druault, Ph., Gaurier, B., 2019a. Experimental investigation of the turbulent wake past real seabed elements for velocity variations characterization in the water column. Int. J. Heat Fluid Flow 78.

[28] Ikhennicheu, M., Germain, G., Druault, Ph., Gaurier, B., 2019b. Experimental study of coherent flow structures past a wall-mounted square cylinder. Ocean Eng. 182, 137–146.

[29] Keane, A., Nisbet, I., Calvo, G., Pickering, G., Tulloch, J., More, G., Koronka, N., 2022. Wind farm cumulative induction zone effect and the impact on energy yield estimation. Renew. Energy 181, 1209–1222.

[30] Kolekar, N., Banerjee, A., 2015. Performance characterization and placement of a marine hydrokinetic turbine in a tidal channel under boundary proximity and blockage effects. Applied Energy 148, 121–133.

[31] Kolekar, N., Vinod, A., Banerjee, A., 2019. On blockage effects for a tidal turbine in free surface proximity. Energies 12, 3325.

[32] Li, C., Abraham, A., Li, B., Hong, J., 2020a. Incoming flow measurements of a utility-scale wind turbine using super-large-scale particle image velocimetry. J. Wind Eng. Ind. Aerodynamics 197, 104074.

[33] Li, C., Abraham, A., Li, B., Hong, J., 2020b. Incoming flow measurements of a utility-scale wind turbine using super-large-scale particle image velocimetry. J. Wind Eng. Ind. Aerodynamics 197, 104074.

[34] Li, L., Liu, Y., Yuan, Z., Gao, Y., 2018. Wind field effect on the power generation and aerodynamic performance of offshore floating wind turbines. Energy 157, 378–390.

[35] Magnier, M., Delette, N., Druault, Ph., Gaurier, B., Germain, G., under review. Experimental study of the shear flow effect on tidal turbine blade loading variation. Renew. Energy 193, 744-757.

[36] Magnier, M., Druault, Ph., Gaurier, B., Germain, G., 2020. Comparison of bathymetry variation effects on tidal turbine behaviour, in: 17èmes journées de l'hydrodynamique, Cherbourg, France.

[37] Magnier, M., Druault, Ph., Germain, G., 2021. Experimental investigation of upstream cube effects on the wake of a wall-mounted cylinder: Wake rising reduction, tke budget and flow organization. Eur. J. Mech. B/Fluids 87, 92–102.

[38] Mann, J., Pena, A., Troldborg, N., Andersen, S., 2018. How does turbulence change approaching a rotor? Wind Energy Science 3, 293–300.

[39] Medici, D., Ivanell, S., Dahlberg, J.Å., Alfredsson, P.H., 2011. The upstream flow of a wind turbine: blockage effect. Wind Energy 14, 691–697.

[40] Meyer Forsting, A., Van der Laan, M., Troldborg, N., 2018. The induction zone/factor and sheared inflow: A linear connection ? J. Phys.: Conf. Series 1037, 072031.

[41] Milne, I.A., Graham, J.M., 2019. Turbulence velocity spectra and intensities in the inflow of a turbine rotor. J. Fluid Mech. 870, 870R31–870R311.

[42] Ouro, P., Harrold, M., Stoesser, T., Bromley, P., 2017. Hydrodynamic loadings on a horizontal axis tidal turbine prototype. J. Fluids Struct. 71, 78–95.

[43] Segalini, A., Dahlberg, J.Å., 2019. Global blockage effects in wind farms. J. Phys.: Conf. Series 1256, 012021.

[44] Sentchev, A., Nguyen, T.D., Furgerot, L., Bailly du Bois, P., 2020. Underway velocity measurements in the Alderney Race: towards a three-dimensional representation of tidal motions. Phil. Trans. R. Soc. A 378, 20190491.

[45] Simley, E., Angelou, N., Mikkelsen, T., Sjöholm, M., Mann, J., Pao, L.Y., 2016. Characterization of wind velocities in the upstream induction zone of a wind turbine using scanning continuous-wave lidars. J. Renew. Sustainable Energy 8.

[46] Slinger, C., Harris, M., Pitter, M., 2020a. Wind speed measurement for absolute power curve determination from induction zone lidar measurements. J. Phys.: Conf. Series 1618, 032027.

[47] Slinger, C., Harris, M., Pitter, M., 2020b. Wind speed measurement for absolute power curve determination from induction zone lidar measurements. J. Phys.: Conf. Series 1618, 032027.

[48] Strickland, J.M.I., Stevens, R.J.A.M., 2020. Effect of thrust coefficient on the flow blockage effects in closely-spaced spanwise-infinite turbine arrays. J. Phys.: Conf. Series 1618, 062069.

[49] Thiébot, J., Coles, D.S., Bennis, A.C., Guillou, N., Neill, S., Guillou, S., Piggott, M., 2020. Numerical modelling of hydrodynamics and tidal energy extraction in the Alderney Race: a review. Phil. Trans. R. Soc. A 378, 20190498.

[50] Wharton, S., Lundquist, J., 2012. Atmospheric stability affects wind turbine power collection. Environ Res. Letters 7, 17–35.

[51] Yang, X., Howard, K., Guala, M., Sotiropoulos, F., 2015. Effects of a three-dimensional hill on the wake characteristics of a model wind turbine. Phys. Fluids 27.